Supplementary Material for

Semiconducting Cu$_x$Ni$_{3-x}$(hexahydroxytriphenylene)$_2$

framework for electrochemical aptasensing of C6 glioma

cells and epidermal growth factor receptor

Chuanpan Guo[a,b], Zhenzhen Li[a], Fenghe Duan[a,b], Zhihong Zhang[a]*, Fabio Marchetti[b*],

Miao Du[a*]

[a]Department of Material and Chemical Engineering, Zhengzhou University of Light

Industry, Zhengzhou, 450002, PR China

[b]School of Science and Technology, Chemistry Section, University of Camerino, Via

S. Agostino 1, 62032, Camerino, MC, Italy

Corresponding authors

E-mail addresses: 2006025@zzuli.edu.cn (Z. Zhang), fabio.marchetti@unicam.it (F.

Marchetti), dumiao@zzuli.edu.cn (M. Du)

Contents

S1. Experimental section

S1.1 Reagents and materials

$Cu(NO_3)_2 \cdot 3H_2O \cdot$ and $Ni(NO_3)_2 \cdot 6H_2O$ were from Aladdin Reagent Co. Ltd. (Shanghai, China). KH_2PO_4, $Na_2HPO_4 \cdot 12H_2O$, KCl, NaCl, $K_3[Fe(CN)_6]$ and $K_4[Fe(CN)_6] \cdot H_2O$ were from Sinopharm Chemical Reagent Co. Ltd. (Beijing, China). Epidermal growth factor receptor (EGFR), immunoglobulin G (IgG), bovine serum albumin (BSA), vascular endothelial growth factor 165 ($VEGF_{165}$), Alpha fetoprotein (AFP), carcinoembryonic antigen (CEA), carbohydrate antigen 125 (CA 125), and carbohydrate antigen 199 (CA 199) were obtained from Solarbio Bioengineering Ltd. Company (Beijing, China). The aptamer sequence, which was from SBS Genetech Co. Ltd. (http://www.sbsbio.com) and used to detect insulin, is as follow: 5′-GTA CTT CCA TTT GTG TTT GCC CGG AGC CTT AGT CTG TTC AAA AGT-3′. All of the chemicals were of analytical reagent grade and used as received. All solutions were prepared with Milli-Q ultrapure water (≥ 18.2 MΩ·cm).

S1.2 Pre-treatment of the bare Au electrode (AE)

The bare Au electrode (AE) with a diameter of 3.0 mm was applied as working electrode and cleaned prior to use. Firstly, the AE was polished with 0.3 and 0.05 μm alumina powder to obtain a mirror-like surface, following by washing thoroughly with piranha solution (H_2SO_4/H_2O_2 = 7/3, v/v) and ethanol, respectively, for 15 min. Afterwards, the AE was washed with Milli-Q water and dried under nitrogen. The AE was electrochemically activated in 0.5 M H_2SO_4 within the potential cycling between −0.2 V and 1.6 V. Finally, the AE was rinsed with Milli-Q water and dried under

nitrogen again, and stored for further use.

S1.3 Preparation of solutions

Phosphate buffered solution (PBS, 0.01 M, pH 7.4) was prepared by mixing 0.24 g KH_2PO_4, 1.44 g $Na_2HPO_4 \cdot 12H_2O$, 0.20 g KCl, and 8.0 g NaCl. The electrolyte solution for electrochemical tests was prepared immediately before use by dissolving 1.65 g $K_3[Fe(CN)_6]$, 2.11 g $K_4[Fe(CN)_6]$, 8.0 g and 7.45 g KCl in 1.0 L of PBS. The stock solutions of aptamer, IgG, BSA, $VEGF_{165}$, AFP, CEA, CA 125, and CA 199 were prepared using PBS. All solutions were prepared immediately before each test and stored at 4 ℃ until use.

S1.4 Basic characterizations

X-ray diffraction (XRD) patterns were taken on a Rigaku D/Max-2500 X-ray diffractometer with Cu Kα radiation (λ = 0.15406 nm). Fourier transform infrared (FT-IR) spectra were recorded on a Bruker TENSOR27 spectrometer. Raman spectra were taken on a Renishaw inVia spectrometer. X-ray photoelectron spectroscopy (XPS) data were collected on an ESCALAB 250Xi spectrometer with an Al Kα X-ray source (1486.6 eV photons). The surface morphology of the materials was taken on JSM-6490LV field emission scanning electron microscope (FE-SEM) and JEOL JEM-2100 high-resolution transmission electron microscopy (HR-TEM) with a field emission gun of 200 kV. The element distribution was measured by elemental mapping coupled with FE-SEM.

S1.5 Electrochemical measurements

Cyclic voltammetry (CV) and electrochemical impedance spectroscopy (EIS)

were conducted on a CHI 660E electrochemical station. A traditional three-electrode system was used in the electrochemical measurements, including a bare or modified AE as the working electrode, an Ag/AgCl (3M KCl) as the reference electrode, and a platinum wire as the auxiliary electrode. CV curves was taken from −0.2 to 0.8 V at a scan rate of 50 mV·s^{-1} in PBS containing 5 mM [Fe(CN)$_6$]$^{3-/4-}$. EIS was carried out within the frequency range of 0.01 Hz–100 kHz with amplitude of 5 mV under open circuit potential of 0.22 V (**Fig. S1**). The EIS spectra were analyzed using ZView2 software obtained from Scribner Associates Incorporated, which utilizes nonlinear least-squares fitting to determine the parameters in the equivalent circuit (**Fig. S1** inset). The equivalent circuit consists of solution resistance (R_s), charge-transfer resistance (R_{ct}), constant-phase element (CPE), and Warburg impedance (W_o).
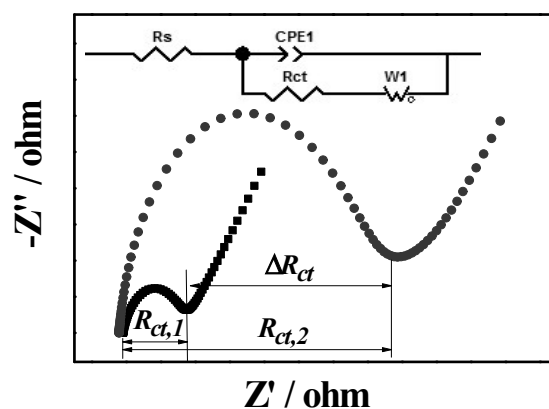
Fig. S1 Typical EIS Nyquist plots and equivalent circuit.

Parameters for tests, including the dosage of Cu$_x$Ni$_{3-x}$(HHTP)$_2$ MOF, concentration of aptamer, and binding time of C6 cells, were determined to obtain the optimal sensing performances. A series of aptasensors were fabricated by modifying

the electrode with $Cu_xNi_{3-x}(HHTP)_2$ MOF at different dosages (0.2, 0.5, 1, 2, and 5 mg·mL^{-1}) to evaluate its effect on sensing performance. $Cu_xNi_{3-x}(HHTP)_2$ MOF/AE was incubated with the aptamer solution at different concentrations (20, 50, 100, 200, and 500 nM) to investigate its influence on the sensitivity of aptasensor. The proposed $Cu_xNi_{3-x}(HHTP)_2$ MOF-based aptasensor was also used to determine C6 cells (1000 cell·mL^{-1}), measured by EIS technique and recorded at different durations to obtain the optimal binding time.

S1.6 Cytotoxicity and in vitro cell uptake

For assessing the cell viability against the MOFs, C6 cells and normal cells of mice, i.e., L929 cells, were cultured in a 96-well plate for 24 h in a humidified atmosphere (5% CO_2, 37 °C). Then, the medium was replaced by the fresh media containing MOFs at various concentrations of 10, 20, 50, 80, and 200 μg·mL^{-1}. After incubating with the suspension of C6 cells for 12 h, the cells were washed with PBS twice, following by adding 200 mL of DMEM media to each well. After further incubating for 12 h at 37 °C, MTT (5 mg·mL^{-1}, 20 μL) was added into each well for culturing for 4 h. Finally, the media was removed and the cells were dispersed in 150 mL of DMSO. Then, the absorbance of each well was measured at 490 and 630 nm using a microplate reader.

Prior to the investigation of in *vitro* cellular uptake, the Cy3-labeled EGFR-targeted aptamer (Cy3-Apt) was immobilized over MOFs, denoted by Cy3-Apt/$Cu_3(HHTP)_2$ MOF, Cy3-Apt/$Ni_3(HHTP)_2$ MOF, and Cy3-Apt/$Cu_xNi_{3-x}(HHTP)_2$ MOF, respectively. Afterwards, L929 and C6 cells were cultured in laser confocal

culture dish for 12 h in a humidified atmosphere (5% CO_2, 37 °C) with a medium containing Cy3-Apt/$Cu_3(HHTP)_2$ MOF, Cy3-Apt/$Ni_3(HHTP)_2$ MOF and Cy3-Apt/$Cu_xNi_{3-x}(HHTP)_2$ MOF. For comparison, the blank experiments were also taken. After the media were removed, the cells were softly rinsed with PBS twice and fixed with 4% paraformaldehyde solution for 15 min. The nuclei were then stained with Hoechst 33342 (20 $\mu g \cdot mL^{-1}$ in PBS) for 20 min and washed with PBS thrice. Finally, the fluorescence images were observed on a confocal laser scanning microscope (CLSM).

S2. Basic characterizations

The XRD patterns of $Cu_3(HHTP)_2$ and $Ni_3(HHTP)_2$ MOFs(**Fig. S2a**) agree well with previous reports [1]. Prominent peaks at 2θ = 4.7°, 9.5°, 12.6° and 16.5° corresponding to (100), (200), (001), and (220) plane, indicate the long-range order within the *ab* plane. Additionally, the broad peaks at 2θ = 27.3° can be indexed to the (002) plane, demonstrating the long-range order along the c direction, as expected for covalently linked layered materials [2-3]. The $Cu_xNi_{3-x}(HHTP)_2$ MOF possesses the identical peak positions with those of $Cu_3(HHTP)_2$ and $Ni_3(HHTP)_2$ MOFs, demonstrating that they are isostructural [4]. The PXRD pattern of the Ni_3HHTP_2 MOF displays an additional diffraction peak around 13.9°, suggesting the alternative stacking mode present in $Ni_3(HHTP)_2$ due to the intercalated layer [5]. Moreover, the FT-IR spectra of $Cu_3(HHTP)_2$, $Ni_3(HHTP)_2$, and $Cu_xNi_{3-x}(HHTP)_2$ MOFs (**Fig. S2b**) show the peaks of –OH at 3400 cm^{-1}, the asymmetric vibration of O=C−O at 1640 and 1436 cm^{-1}, and C–O at 1308 and 1218 cm^{-1}. The characteristic peaks of Cu–O appear at 568 cm^{-1} in $Cu_3(HHTP)_2$ and $Cu_xNi_{3-x}(HHTP)_2$ MOFs. An extremely weak peak at 464 cm^{-1} of $Ni_3(HHTP)_2$ is due to Ni–O, which suggests that the coordination of Cu^{2+} with HHTP is dominant in formation of $Cu_xNi_{3-x}(HHTP)_2$ MOF.
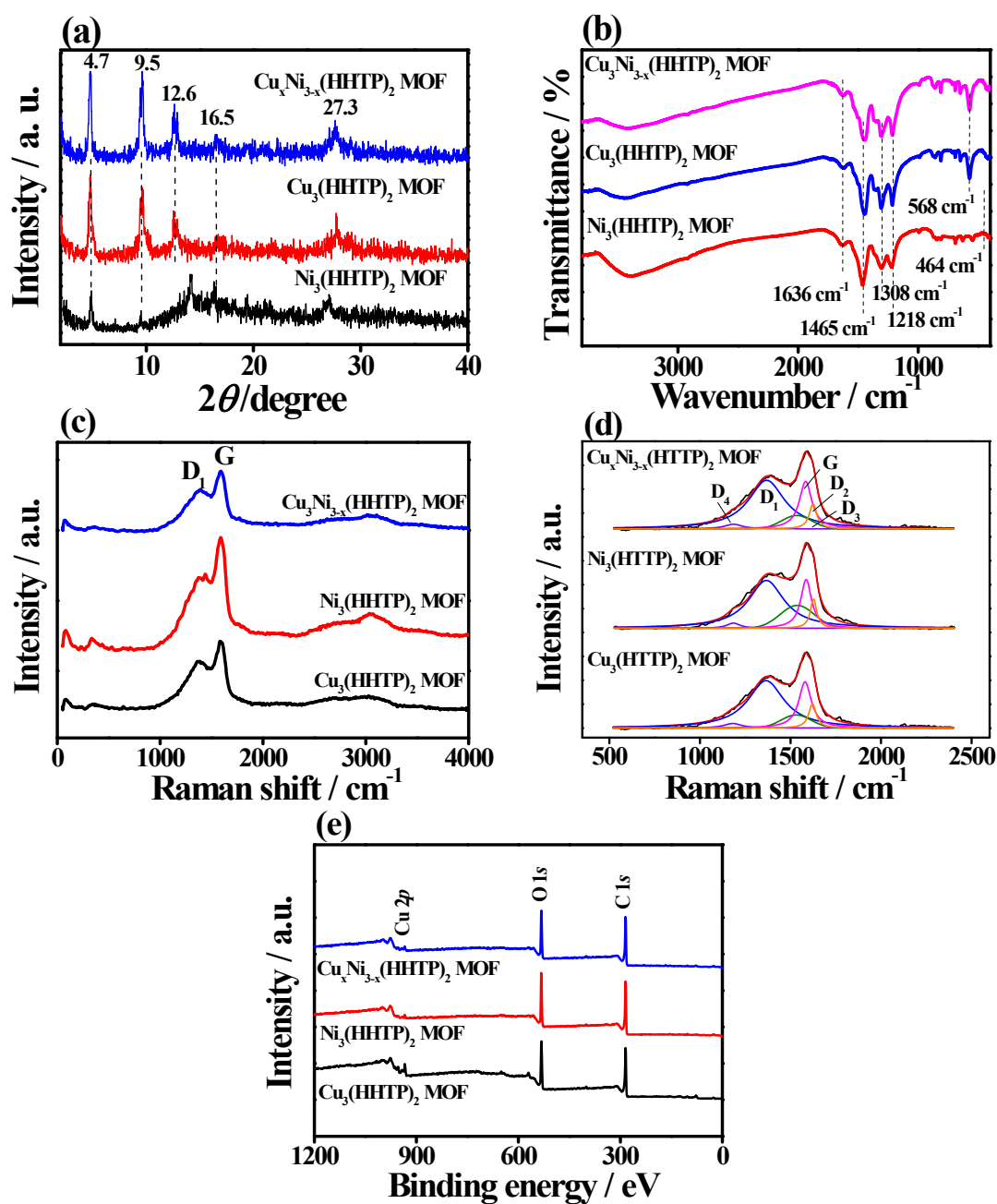
Fig. S2 (a) XRD patterns, (b) FT-IR, (c) Raman, (d) Raman with Gaussian split-peak fitting, and (e) XPS survey scan spectra of $Cu_3(HHTP)_2$, $Ni_3(HHTP)_2$, and $Cu_xNi_{3-x}(HHTP)_2$ MOFs.

The Raman spectra of $Cu_3(HHTP)_2$, $Ni_3(HHTP)_2$, and $Cu_xNi_{3-x}(HHTP)_2$ MOFs (**Fig. S2c**) show the Raman-allowed first-order G band at about 1580 cm^{-1} and the so-

called disorder-induced D_1 band at ca. 1350 cm^{-1} of the graphene-like nanostructure [6].

The weak and broad peaks at 2720 and 3180 cm^{-1} can be assigned to the 2D and 2D′

peaks, respectively [7]. These results reveal that the as-obtained 2D MOFs exhibit

graphene-like structure. For further analysis, five-band fitting procedures were applied

to three MOFs, as shown in **Fig. S2d**. Apart from the G band at ~1580 cm^{-1}, other

four bands of D_1, D_2, D_3 and D_4, which are typically for disordered carbon structure,

are observed at ~1360 cm^{-1}, ~1620 cm^{-1}, ~1530 cm^{-1} and ~1180 cm^{-1}, respectively [8-9].

The area ratios of D_1/G of $Cu_3(HHTP)_2$ and $Ni_3(HHTP)_2$ MOFs are 3.036 and 3.257,

respectively, greater than that of $Cu_xNi_{3-x}(HHTP)_2$ MOF (2.957), hinting that the

$Cu_xNi_{3-x}(HHTP)_2$ MOF exhibits low defective structure with a high degree of

graphitization [10]. It further reveals that the introduction of Ni ions can improve the

graphitization of semiconducting MOF, which can boost the conductivity of the MOF

network [11] and aptamer immobilization [12].
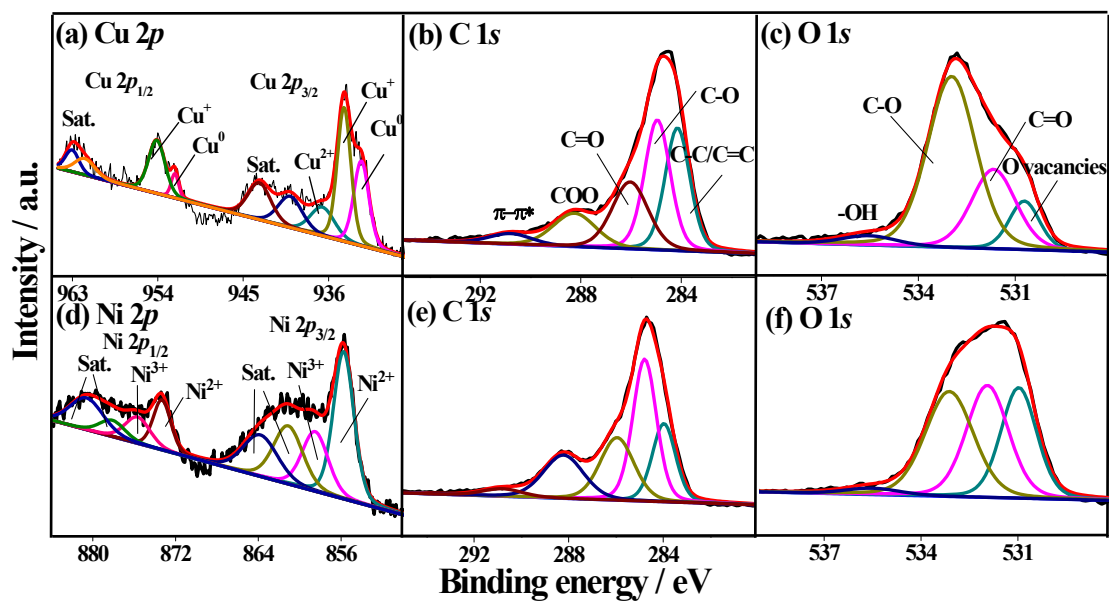
Fig. S3 High-resolution (a) Cu $2p$, (b) C $1s$, and (c) O $1s$ XPS spectra of $Cu_3(HHTP)_2$ MOF and (d) Ni $2p$, (e) C $1s$, and (f) O $1s$ XPS spectra of $Ni_3(HHTP)_2$ MOF.
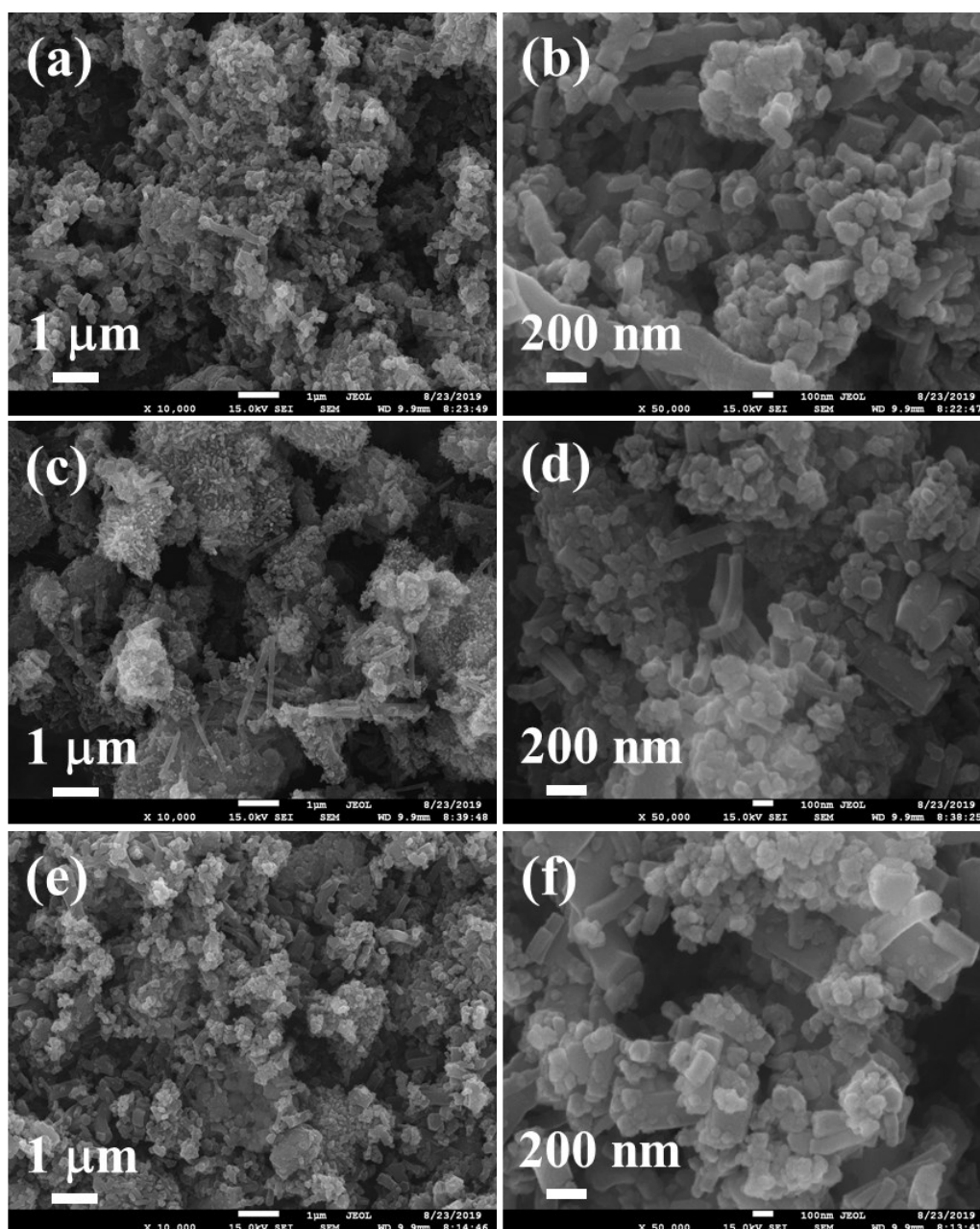
Fig. S4 Low- and high-magnification SEM images of the (a, b) $Cu_3(HHTP)_2$, (c, d) $Ni_3(HHTP)_2$, and (e, f) $Cu_xNi_{3-x}(HHTP)_2$ MOFs.
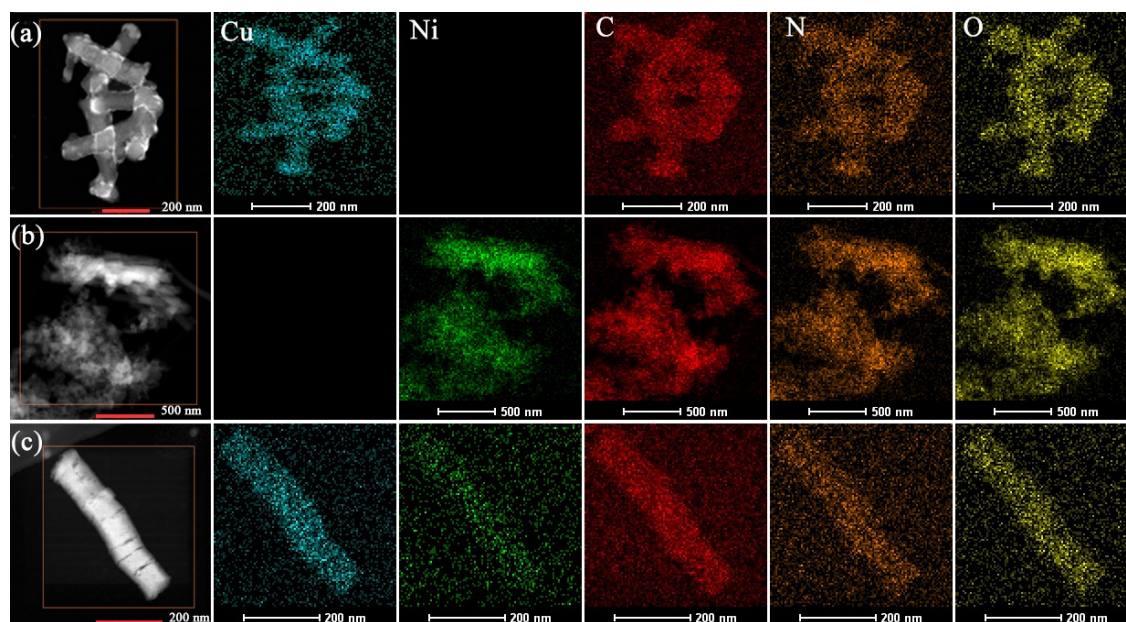
Fig. S5 Elemental mapping of homogenously distributed Cu (blue), Ni (green), C (red), N (brown), and O (yellow) containing in (a) $Cu_3(HHTP)_2$, (b) $Ni_3(HHTP)_2$, and (c) $Cu_xNi_{3-x}(HHTP)_2$ MOFs.
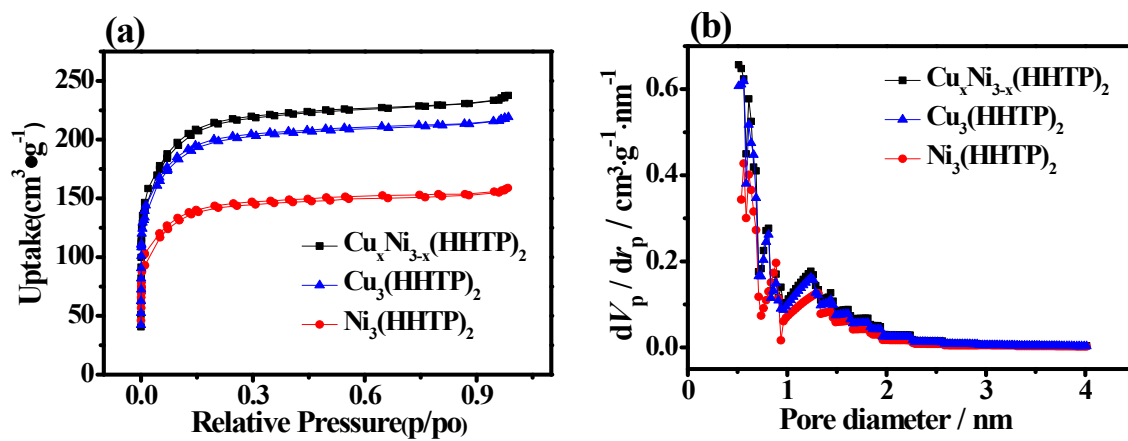
Fig. S6 (a) Nitrogen adsorption-desorption isotherms and (b) pore size distribution of

$Cu_3(HHTP)_2$, $Ni_3(HHTP)_2$, and $Cu_xNi_{3-x}(HHTP)_2$ MOFs.

S3. Determination of C6 cells using the proposed aptasensors
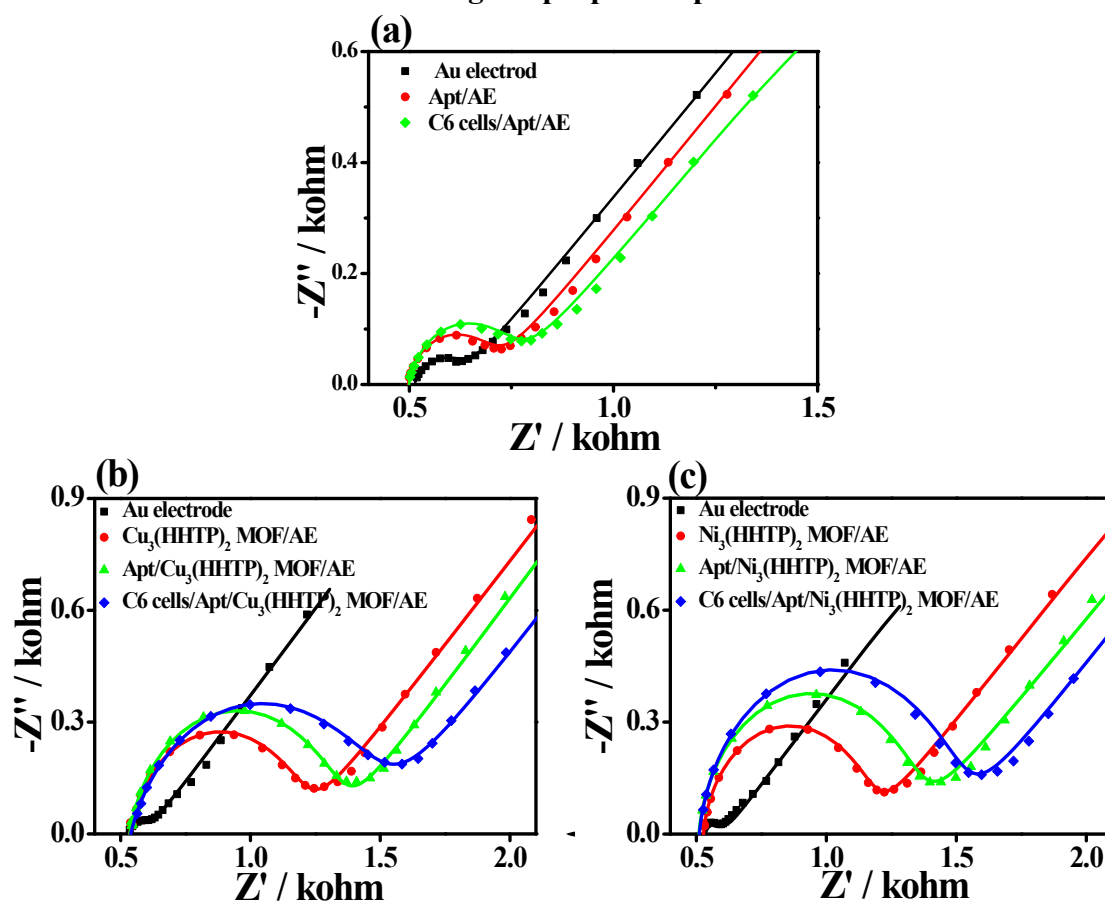
Fig. S7 EIS Nyquist plots of (a) the bare Au electrode, (b) $Cu_3(HHTP)_2$ MOF, and (c) $Ni_3(HHTP)_2$ MOF modified Au electrodes for detecting C6 cells in PBS containing 5.0 mM $[Fe(CN)_6]^{3-/4-}$.
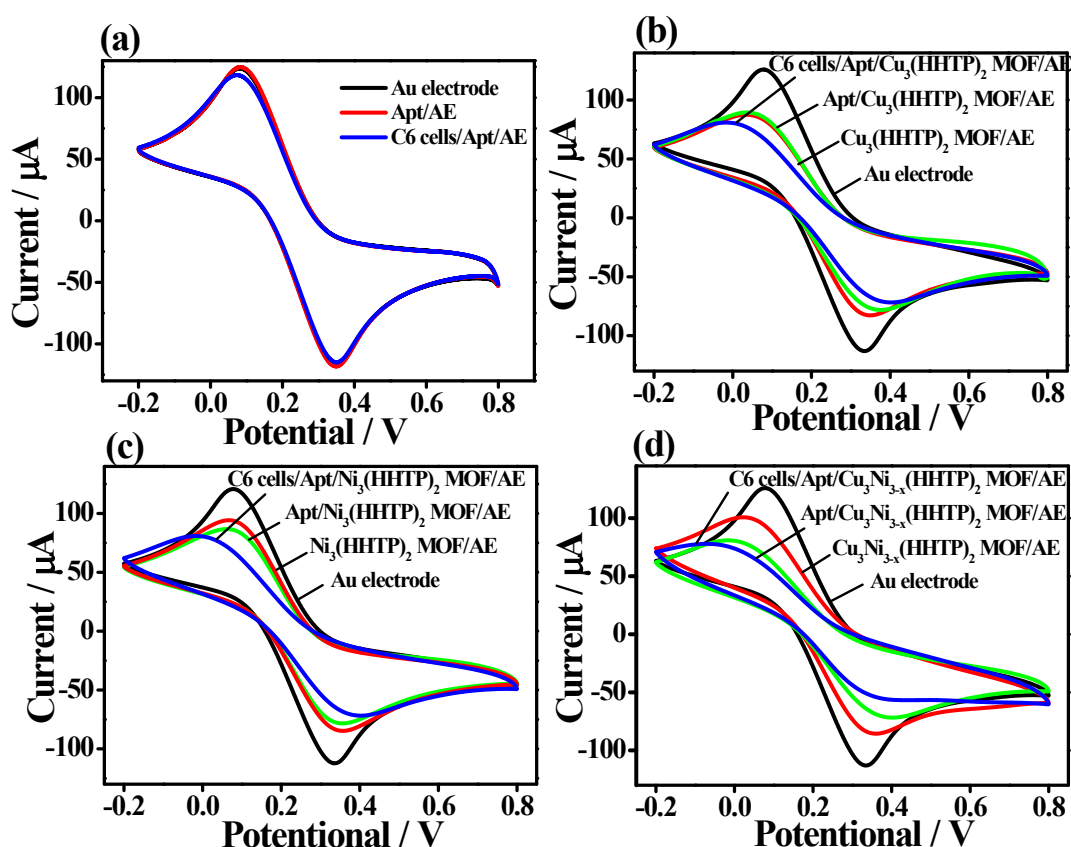
Fig. S8 CV curves of the aptasensors based on (a) the bare Au electrode, (b) $Cu_3(HHTP)_2$, (c) $Ni_3(HHTP)_2$, and (d) $Cu_xNi_{3-x}(HHTP)_2$ MOFs for detecting C6 cells in PBS containing 5.0 mM $[Fe(CN)_6]^{3-/4-}$.

The CV curve (**Fig. S8**) of AE shows typical quasi-reversible oxidation and reduction wave peaks of $[Fe(CN)_6]^{3-/4-}$, which acts as redox-active probe to indicate the electron transfer between electrolyte and working electrode [13]. Regarding $Cu_xNi_{3-x}(HHTP)_2$ MOF/AE, the enclosed area of CV curve becomes smaller than AE, and peak current density also decreases. These results suggest that $Cu_xNi_{3-x}(HHTP)_2$ MOF slightly hinders the electron transfer at the electrode/electrolyte interface [14]. The $Apt/Cu_xNi_{3-x}(HHTP)_2/AE$ displays a reduced enclosed area and peak current density. The aptamer strand can be ionized in water, which leads to the production of the

negative charge of phosphate groups. Thus, a strong repulsion between the negative charge of phosphate groups and $[Fe(CN)_6]^{3-/4-}$ can prevent the electron transferring, resulting in a decrease of the electrochemical activity for the electrode [15]. The current density of CV curve of $C6/Apt/Cu_xNi_{3-x}(HHTP)_2$ MOF/AE continuously declines, suggesting the strong binding between aptamer strands and C6 cells [16]. Further, aptasensors based on $Cu_3(HHTP)_2$ and $Ni_3(HHTP)_2$ MOFs were investigated for detecting C6 cells using CV technique. The change trend in their peak current density and enclosed area is very close, revealing similar sensing performances. The dissimilarity among CV curves clearly suggests different detection ability or sensitivity of the three kinds of aptasensors.

Table S1 R_{ct} values of each step during the detection procedures for C6 cells (1000 cell mL^{-1}) using the cytosensors based on Cu$_3$(HHTP)$_2$, Ni$_3$(HHTP)$_2$, and Cu$_x$Ni$_{3-x}$(HHTP)$_2$ MOFs.

R_{ct} (Ω)	Electrode materials		
	Cu$_3$(HHTP)$_2$	Ni$_3$(HHTP)$_2$	Cu$_3$Ni$_{3-x}$(HHTP)$_2$
AE	120	118	120.3
RSD% (n=3)	3.8	2.6	1.8
Materials/AE	707	689	381.3
RSD% (n=3)	2.9	2.9	3.8
Apt/Materials/AE	845.4	877.4	682.3
RSD% (n=3)	4.1	1.9	2.6
C6/Apt/Materials/AE	998.4	1039.4	1098.3
RSD% (n=3)	3.5	4.7	2.4
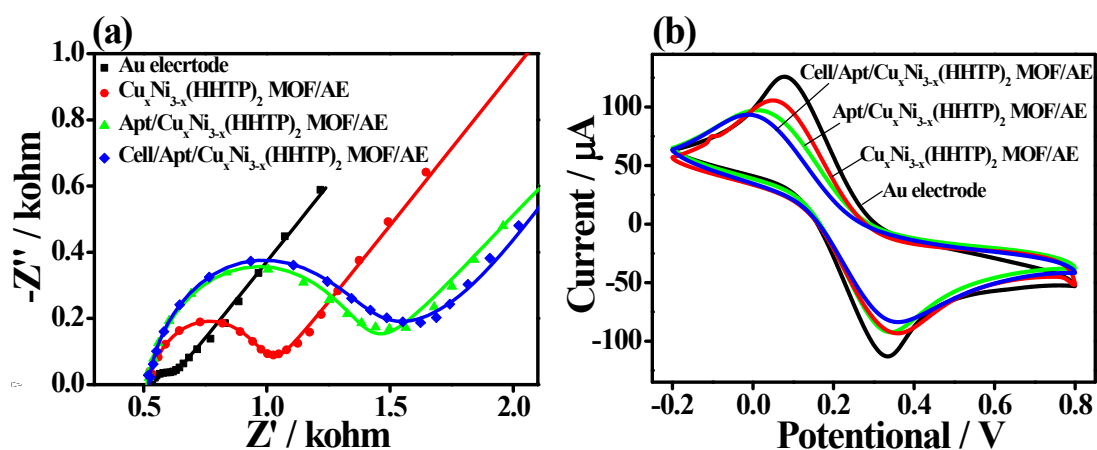
Fig. S9 (a) EIS Nyquist plots and (b) corresponding CV curves for the $Cu_xNi_{3-x}(HHTP)_2$ MOF-based aptasensor for detecting L929 cells (1×10^5 cell mL^{-1}) in PBS containing 5.0 mM $[Fe(CN)_6]^{3-/4-}$.
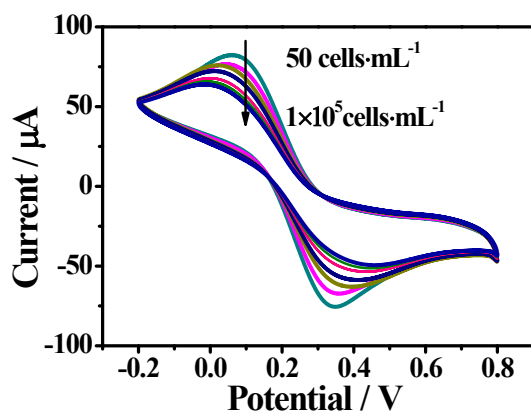
Fig. S10 CV curves of Apt/$Cu_xNi_{3-x}(HHTP)_2$/AE toward C6 cells with different concentrations (0, 50, 1×10^2, 5×10^2, 1×10^3, 5×10^3, 1×10^4, 5×10^4, and 1×10^5 cells mL^{-1}).

Table S2 Detection of C6 cells in human serum using the $Cu_xNi_{3-x}(HHTP)_2$ MOF-based cytosensor.

Amount added (cells·mL^{-1})	ΔR_{ct} (kohm)	Found (cells·mL^{-1})	Apparent recovery (%)	RSD (%)
50	0.159	53	106	3.18
1×10^2	0.234	108	108	2.67
5×10^2	0.400	527	105.4	4.36
1×10^3	0.467	994	99.4	2.86
5×10^3	0.645	5367	107.3	1.59
1×10^4	0.712	10187	101.9	1.76
5×10^4	0.882	51684	103.4	2.56
1×10^5	0.867	105418	105.4	3.46

S4. Optimization of experimental parameters for detecting C6 cells
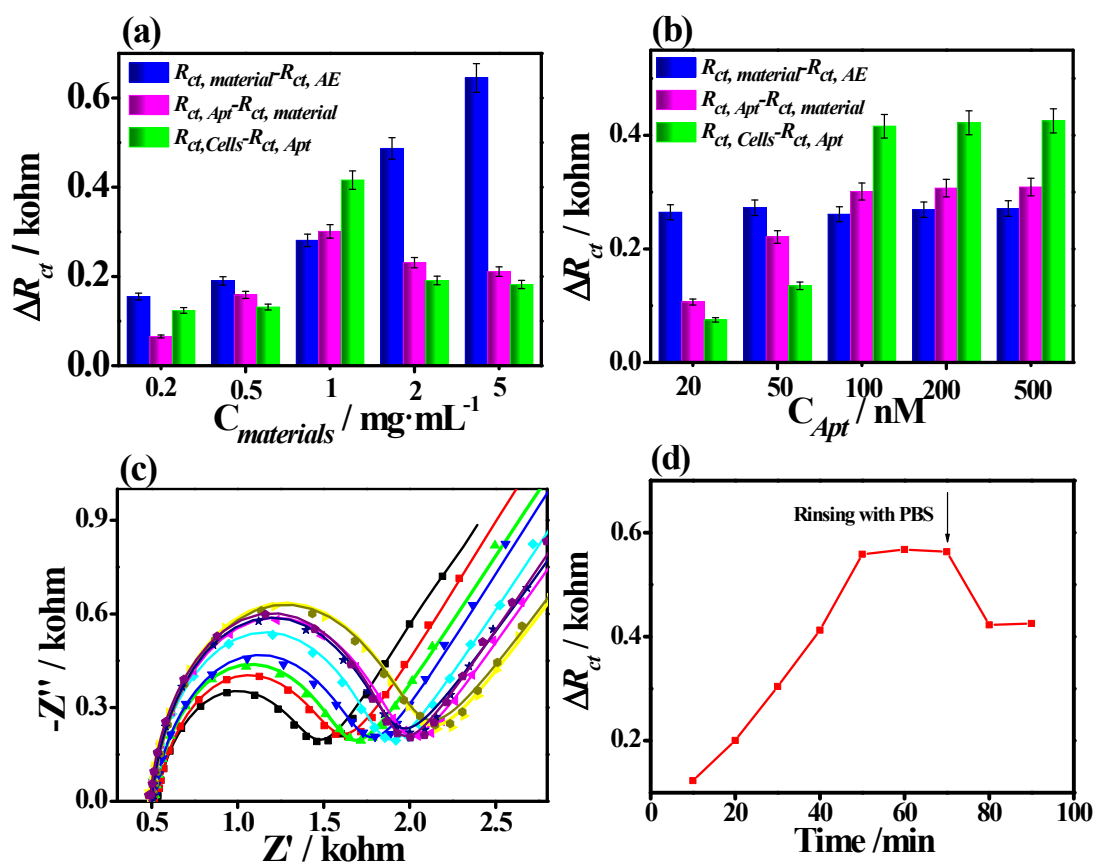
Fig. S11 Effect of (a) the dosage of $Cu_xNi_{3-x}(HHTP)_2$ MOF and (b) the concentration of aptamer strands on the variation of R_{ct} values before and after detecting C6 cells. (c) EIS Nyquist plots of the $Cu_xNi_{3-x}(HHTP)_2$ MOF-based aptasensor incubated with C6 cells (1000 cell·mL^{-1}) for different durations and (d) their corresponding ΔR_{ct} values.

Screening the experimental parameters for electrochemical measurements, such as the dosage of $Cu_xNi_{3-x}(HHTP)_2$ MOF, the aptamer concentration, and the binding time toward C6 cells, is essential to achieve the optimal sensing performances. A series of $Cu_xNi_{3-x}(HHTP)_2$ MOF-based aptasensors were constructed under the same condition by using different dosages of $Cu_xNi_{3-x}(HHTP)_2$ MOF (0.2, 0.5, 1.0, 2.0, and

5.0 mg·mL^{-1}) for determining C6 cells (1×10^3 cells·mL^{-1}). The ΔR_{ct} value before and after modification of AE with Cu$_x$Ni$_{3-x}$(HHTP)$_2$ MOF increases along with increasing its dosage (**Fig. S11a**). This observation reveals that the thick Cu$_x$Ni$_{3-x}$(HHTP)$_2$ MOF layer can substantially hinder the electron transfer at the solid/liquid interface. However, the ΔR_{ct} values stimulated by aptamer immobilization and C6 cells detection first arises with the increasing Cu$_x$Ni$_{3-x}$(HHTP)$_2$ MOF dosage from 0.2 to 1 mg·mL^{-1}, and then declines when the Cu$_x$Ni$_{3-x}$(HHTP)$_2$ MOF dosage is larger than 1.0 mg·mL^{-1}. During the electrochemical measurement, it can be observed that partial Cu$_x$Ni$_{3-x}$(HHTP)$_2$ MOF will be released from the electrode surface (Cu$_x$Ni$_{3-x}$(HHTP)$_2$ MOF dosage: 2.0 mg·mL^{-1}), which reveals that excessively thick MOF layer is not stable in water. As a result, Cu$_x$Ni$_{3-x}$(HHTP)$_2$ MOF with a concentration of 1.0 mg·mL^{-1} is selected to develop the cytosensor.

Prior to detecting C6 cells, the Cu$_x$Ni$_{3-x}$(HHTP)$_2$ MOF-based cytosensors were separately incubated with the aptamer solutions at different concentrations of 20, 50, 100, 200, and 500 nM. The ΔR_{ct} values for each cytosensor (**Fig. S11b**) show a continuous increase, with increasing the concentration of aptamer in the range of 20–100 nM. After that, the ΔR_{ct} values reach an equilibrium, which suggests a saturated binding between the aptamer strands and C6 cells. Thus, the aptamer solution of 100 nM is selected to test the electrochemical sensing.

To evaluate the influence of incubation time of C6 cells on the sensing performance, the EIS Nyquist plots for the proposed Cu$_x$Ni$_{3-x}$(HHTP)$_2$ MOF-based cytosensor were recorded (**Fig. S11c**). The observed ΔR_{ct} value increased with the

prolonged binding time of C6 cells. This finding remains at a level-off when the binding time is longer than 50 min, which implies the statured combination of aptamer and C6 cells. When washing the sensing system using excessive PBS, the ΔR_{ct} value will decrease, because some loosely adsorbed aptamer-C6 complexes fall off (**Fig. S11d**).

S6. Determination of EGFR using the proposed aptasensors
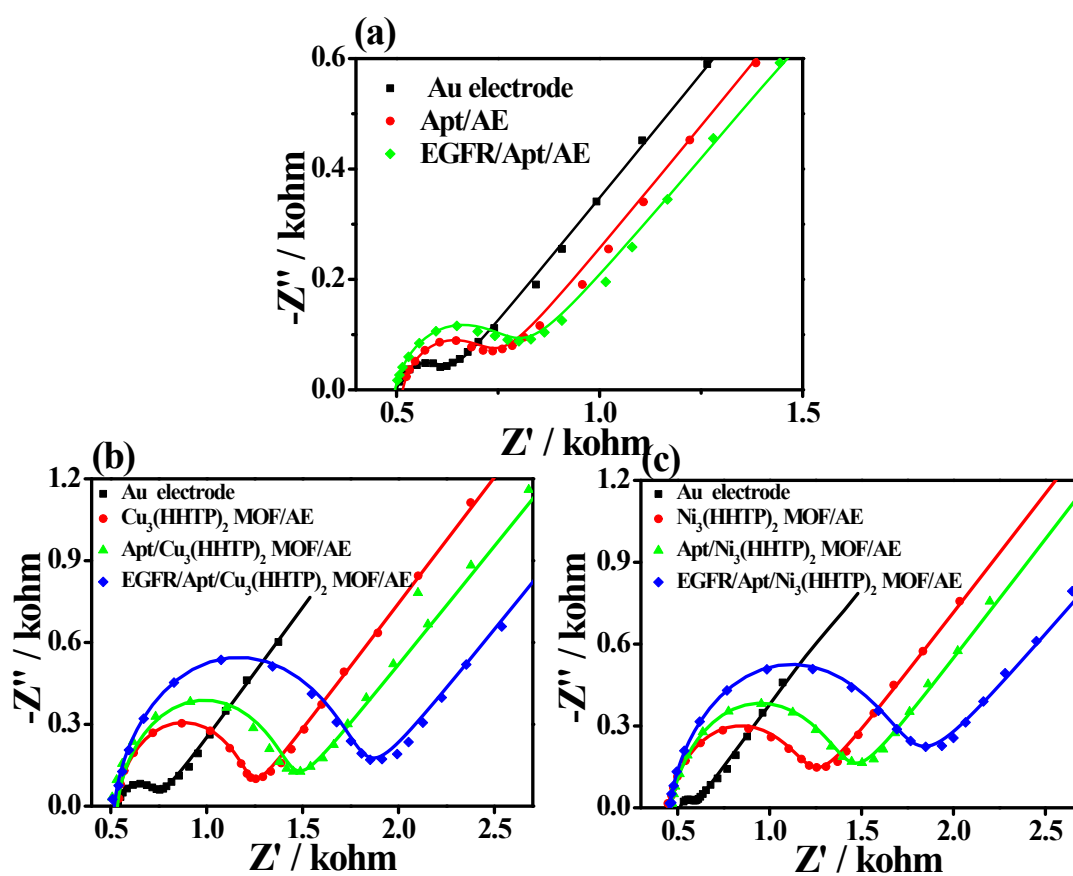
Fig. S12 EIS Nyquist plots of the aptasensors based on of (a) the bare Au electrode, (b) $Cu_3(HHTP)_2$, and (c) $Ni_3(HHTP)_2$ MOFs for detecting EGFR (1 pg·mL^{-1}) in PBS containing 5.0 mM $[Fe(CN)_6]^{3-/4-}$.

Fig. S13 (a) EIS Nyquist plots of the $Cu_xNi_{3-x}(HHTP)_2$ MOF-based aptasensor incubated with EGFR (1 pg·mL^{-1}) for different durations and (b) their corresponding ΔR_{ct} values.

To evaluate the influence of incubation time of EGFR on the sensing performance, the EIS Nyquist plots for the proposed $Cu_xNi_{3-x}(HHTP)_2$ MOF-based aptasensor were recorded (**Fig. S13**). The observed $\D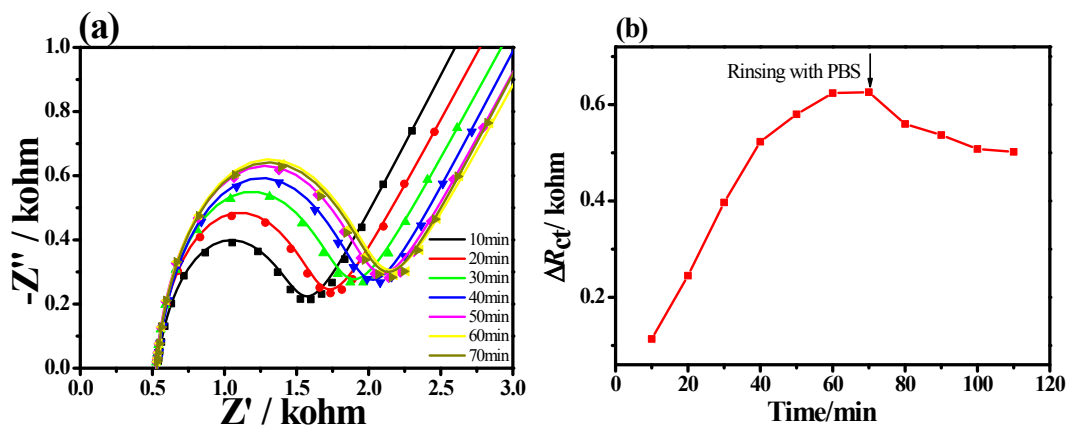elta R_{ct}$ value increased with the prolonged binding time of EGFR and reach the plateau up to 60 min, which implies the statured combination of EGFR. Therefore, the optimal experimental parameter for cells binding was 60 min. When rinsing with PBS, the electrochemical response decreases and approaches to a platform again. It hints that some loosely adsorbed aptamer-EGFR complexes release from the matrix.

Table S3 R_{ct} values of each step during the detection procedures for EGFR using the aptasensors based on $Cu_3(HHTP)_2$, $Ni_3(HHTP)_2$, and $Cu_xNi_{3-x}(HHTP)_2$ MOFs.

R_{ct} (Ω)	Electrode materials		
	$Cu_3(HHTP)_2$	$Ni_3(HHTP)_2$	$Cu_3Ni_{3-x}(HHTP)_2$
AE	115	120.5	117
RSD% (n=3)	2.6	2.7	3.5
Materials/AE	700.4	758.1	394.6
RSD% (n=3)	3.1	1.5	2.8
Apt/Materials/AE	888.2	889.2	692.9
RSD% (n=3)	1.3	2.4	4.2
EGFR/Apt/Materials/AE	1262.9	1213.5	1318.7
RSD% (n=3)	3.8	2.7	3.4
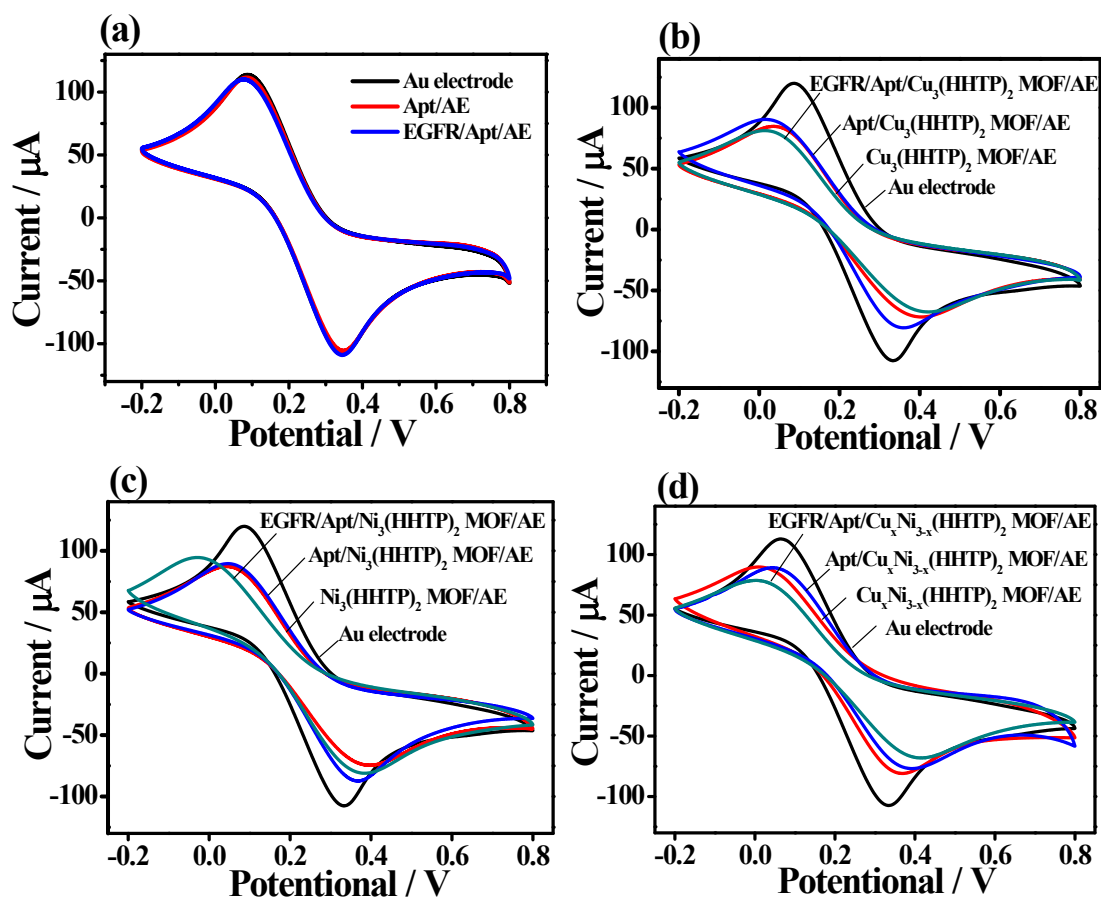
Fig. S14 CV curves of the aptasensors based on (a) the bare Au electrode, (b) $Cu_3(HHTP)_2$, (c) $Ni_3(HHTP)_2$, and (d) $Cu_xNi_{3-x}(HHTP)_2$ MOFs for detecting EGFR (1 pg·mL^{-1}) in PBS containing 5.0 mM $[Fe(CN)_6]^{3-/4-}$.

Table S4 Comparison with the reported sensing techniques for detection of EGFR.

Materials	Detection method	Detection range (pg·mL^{-1})	LOD (fg·mL^{-1})	Refs.
Cysteamine/PDITC/protein G/gold nanoparticles	Impedimetry	1–10^6	340	[17]
CMK3-p(AC-co-MDHLA)-Ab$_{EGFR}$-AMS	Amperometry	10–5×10^4	3030	[18]
MIP-AbEGFR-Cd(II)@LP-AbVEGF-Cu(II)@LP	Potentiometric stripping analysis	0.05–5×10^4	10	[19]
primer 1 + primer 2	Fluorescence	0.17–1.7×10^5	27.2	[20]
Ferrocene-labeled peptide ligand	DPV	0.1–1×10^3	37	[21]
Fe$_3$O$_4$/N-trimethyl chitosan/Au	DPV	0-10^3	50	[22]
p-COF	DPV	0.05–100	5.64	[23]
Cu$_x$Ni$_{3-x}$(HHTP)$_2$ MOF	**EIS**	**0.001–2×10^3**	**0.72**	**This work**

Table S5 Detection of EGFR in human serum sample by the $Cu_xNi_{3-x}(HHTP)_2$ MOF-based electrochemical aptasensor.

Amount added (fg·mL^{-1})	ΔR_{ct} (kohm)	Found (fg·mL^{-1})	Recovery (%)	RSD (%)
0.001	0.172	0.00103	103.0	2.92
0.01	0.458	0.0984	98.4.	4.18
0.1	0.463	0.106	106	3.67
1	0.600	0.957	95.7	2.35
10	0.748	10.232	102.3	2.13
100	0.892	102.1	102.1	1.05
1000	1.035	1007	100.7	1.57
2000	1.179	10054	100.54	1.10

References

1. H. Bastian, D. J. Karen, D. Hindricks and S. Hendrik A, *Cryst EngComm*, 2019, **20**, 6458-6471.

2. M. Hmadeh, Z. Lu, Z. Liu, F. Gándara, H. Furukawa, S. Wan, V. Augustyn, R. Chang, L. Liao, F. Zhou, E. Perre, V. Ozolins, K. Suenaga, X. Duan, B. Dunn, Y. Yamamto, O. Terasaki and O. M. Yaghi, *Chem. Mater.*, 2012, **24**, 3511-3513.

3. D. Sheberla, L. Sun, M. A. Blood-Forsythe, S. Er, C. R. Wade, C. K. Brozek, A. Aspuru-Guzik and M. Dincă, *J. Am. Chem. Soc.*, 2014, **136**, 8859-8862.

4. W. Li, J. Lv, Q. Li, J. Xie, N. Ogiwara, Y. Huang, H. Jiang, H. Kitagawa, G. Xu and Y. Wang, *J. Mater. Chem. A*, 2019, **7**, 10431-10438.

5. M. Ko, L. Mendecki, A. M. Eagleton, C. G. Durbin, R. M. Stolz, Z. Meng and K. A. Mirica, *J. Am. Chem. Soc.*, 2020, **142**, 11717-11733.

6. M. Yao, X. Lv, Z. Fu, W. Li, W. Deng, G. Wu and G. Xu, *Angew. Chem. Int. Edit.*, 2017, **56**, 16510-16514.

7. M. K. Smith, K. E. Jensen, P. A. Pivak and K. A. Mirica, *Chem. Mater.*, 2016, **28**, 5264-5268.

8. N. P. Ivleva, A. Messerer, X. Yang, R. Niessner and U. Pöschl, *Environ. Sci. Technol.*, 2007, **41**, 3702-3707.

9. P. Parent, C. Laffon, I. Marhaba, D. Ferry, T. Z. Regier, I. K. Ortega, B. Chazallon, Y. Carpentier and C. Focsa, *Carbon*, 2016, **101**, 86-100.

10. Y. Wang, X. Liang, G. Tang, Y. Chen, L. Dong and G. Shu, *Fuel*, 2017, **190**, 237-244.

11. J. Xu, J. Xia, F. Zhang and Z. Wang, *Electrochim. Acta*, 2017, **251**, 71-80.

12. F. Gao, L. Du, Y. Zhang, F. Zhou and D. Tang, *Biosens. Bioelectron.*, 2016, **86**, 185-193.

13. X. Liu, M. Hu, M. Wang, Y. Song, N. Zhou, L. He and Z. Zhang, *Biosens. Bioelectron.*, 2019, **123**, 59-68.

14. M. Gauthier, T. J. Carney, A. Grimaud, L. Giordano, N. Pour, H. Chang, D. P. Fenning, S. F. Lux, O. Paschos, C. Bauer, F. Maglia, S. Lupart, P. Lamp and Y. Shao-Horn, *J. Phys. Chem. Lett.*, 2015, **6**, 4653-4672.

15. M. Dahbi, N. Yabuuchi, M. Fukunishi, K. Kubota, K. Chihara, K. Tokiwa, X. Yu, H. Ushiyama, K. Yamashita, J. Son, Y. Cui, H. Oji and S. Komaba, *Chem. Mater.*,

2016, **28**, 1625-1635.

16. Y. Li, K. Leung and Y. Qi, *Accounts Chem. Res.*, 2016, **49**, 2363-2370.

17. R. Elshafey, A. C. Tavares, M. Siaj and M. Zourob, *Biosens. Bioelectron.*, 2013, **50**, 143-149.

18. M. Regiart, M. A. Fernández-Baldo, J. Villarroel-Rocha, G. A. Messina, F. A. Bertolino, K. Sapag, A. T. Timperman and J. Raba, *Anal. Chim. Acta*, 2017, **963**, 83-92.

19. M. Johari-Ahar, P. Karami, M. Ghanei, A. Afkhami and H. Bagheri, *Biosens. Bioelectron.*, 2018, **107**, 26-33.

20. D. Zhang, F. Ma, Q. Zhang and C. Zhang, *Chem. Commun.*, 2017, **53**, 11496-11499.

21. R. Li, H. Huang, L. Huang, Z. Lin, L. Guo, B. Qiu and G. Chen, *Electrochim. Acta*, 2013, **109**, 233-237.

22. K. Omidfar, M. Darzianiazizi, A. Ahmadi, M. Daneshpour and H. Shirazi, *Sensor. Actuat. B-Chem.*, 2015, **220**, 1311-1319.

23. X. Yan, Y. Song, J. Liu, N. Zhou, C. Zhang, L. He, Z. Zhang and Z. Liu, *Biosens. Bioelectron.*, 2019, **126**, 734-742.